Acta Materialia 195 (2020) 482–490

Contents lists available at ScienceDirect

Acta Materialia

journal homepage: www.elsevier.com/locate/actamat

Full length article

Fabrication of bimorph lead zirconate titanate thick films on metal substrates via the cold sintering-assisted process

Dixiong Wang*, Sinan Dursun, Lisheng Gao, Carl S. Morandi, Clive A. Randall, Susan Trolier-McKinstry

Department of Materials Science and Engineering and Materials Research Institute, The Pennsylvania State University, University Park, PA 16802, USA

ARTICLE INFO

Article History:
Received 13 January 2020
Revised 14 April 2020
Accepted 22 May 2020
Available online 30 May 2020

Keywords:
Lead zirconate titanate
Cold sintering
Co-firing
Piezo MEMS
Energy harvester

ABSTRACT

A novel process was developed for the fabrication of 5–50 μm lead zirconate titanate (PZT) thick films on metal substrates. Tape cast PZT with a methyl cellulose binder was burned out at 275 °C, humidified, and then partially densified at 300 °C by cold sintering with a wet lead nitrate liquid phase. Lamination of the green tape on dense metal foils led to incomplete densification due to constrained sintering. However, when metal foils were replaced with tape cast Cu, fully sintered PZT/Cu/PZT composites were acquired after a secondary heat treatment at 800 °C. The PZT films has a relative permittivity over 500 and a loss tangent ~12% at 100 Hz because of a Cu_2O interface between the PZT and Cu presumably formed during the cold sintering process. The polarization-electric field hysteresis loop shows a remanent polarization over 20 $\mu C/cm^2$, and the $e_{31,f}$ of the samples is -4.7 C/m^2.

1. Introduction

The internet of things (IoT) is driving an evolution in which individual devices that seldom communicate with each other are being replaced by those driven by inter-device collaboration and information sharing. [1] Therefore, demands for sensors and actuators that collect and share data are growing. Powering these devices remains challenging due to the sheer number of devices; utilizing these devices in all-weather conditions or as body implants compounds these challenges. However, self-powered devices utilizing energy harvesters show promise and are gaining attention.

There are a number of ways to scavenge energy from the environment. Sunlight [2], wind [3], tide [4], and geothermal heat [5] energies have been employed for decades. These sources are suitable for infrastructure power supplies but have limited potential in implantable devices. However, piezoelectric electromechanical energy harvesters (PEH) have been utilized successfully in wearable and implanted devices that are small, low power, and isolated from the external environment [6,7]. As piezoelectric ceramics are readily fabricated, they are widely utilized in PEHs. This is abetted by the fact that the production costs of ceramics are significantly smaller than single crystals of the same composition, and the power output of ceramic PEH is higher than that of polymer piezoelectrics [8].

In PEHs, cantilever structures have been widely adopted for low power wearable and implantable electronics; [9] in these devices, when the beams are strained, power can be generated using the piezoelectric as the transducer. Specifically for a "31" mode cantilever PEH, in cases of which a z-direction polarization is generated from strains in the x-y plane, the power of the PEH can be calculated by the following equation: [10]

$$P_{rms} = \frac{\omega}{4}\left(\frac{e_{31}^2}{\varepsilon_0 \varepsilon_r}\right)(At)S^2 \quad (1)$$

where P_{rms} is the root mean square (RMS) power, ω is the angular velocity of the vibration, e_{31} is the transverse piezoelectric constant, ε_0 is the vacuum permittivity, ε_r is the relative dielectric constant of the piezoelectric layer, A and t are the active area/thickness of the piezoelectric materials, and S is the zero to peak strain level.

Multiple approaches have been adopted to increase the output power of a PEH. The first is to optimize the materials figure of merit $\frac{e_{31}^2}{\varepsilon_r}$, which is often approximated by $\frac{e_{31,f}^2}{\varepsilon_r}$. Randomly oriented bulk lead zirconate titanate (PZT) typically have $e_{31,f}$ from −10 to −30 C/m^2 depending on the compositions but the permittivities of PZT are well above 1000. [11,12] As a consequence, the FoM for PZT ceramics are typically below 0.15 C^2/m^4. Some improvements have been reported in textured perovskite ceramics [13]. This can be substantially increased to ~ 1 C^2/m^4 by domain engineering PZT films [13], though this approach is typically limited in terms of the achievable piezoelectric volume [8,14]. Despite the modest piezoelectric coefficients (~3 C/m^2), c-oriented *Sc*-doped AlN thin films have a FoM over 0.5 C^2/m^4 due to the low permittivity ~18; [15] again, there are significant challenges in increasing the thickness beyond a few microns without loss of orientation.

* Corresponding author.
E-mail address: dow5263@psu.edu (D. Wang).

https://doi.org/10.1016/j.actamat.2020.05.053
1359-6454/

As an alternative approach, the volume of the piezoelectric can be increased, since many thin film harvesters, in particular, are under coupled [10]. Bimorph construction (in which piezoelectrics are attached to both sides of the structure) is commonly used so as to maximize the area or thickness of the piezoelectrics [16]. Beside amplifying the power output, the piezoelectric thicknesses also control the output voltage for PEH [14]:

$$V_{OC} = S_x h_{31,f} t \quad (2)$$

Where V_{OC} is the open-circuit voltage, S_x is the in-plane strain, $h_{31,f}$ is the effective piezoelectric voltage constant, and t is the thickness of the piezoelectric layer. The magnitude of the open-circuit voltage is important because the output from a PEH needs to be rectified, and most rectifying circuits require a threshold voltage to operate. [17] The voltages from thin film harvesters are often too low for rectification due to the small thickness, while that harvested from the bulk piezoelectrics are often too large for easy recharging of batteries.

Finally, power output can also be increased if the strain imposed on the PEH is increased for the whole volume of the piezoelectric. This has been done through use of trapezoidal-shaped cantilevers [18] or the piezoelectric compliance mechanism (PCM) design [19], both of which homogenize the strain distribution across the energy harvester beams. Typically, bulk piezoelectric materials provide high voltages with low power densities due to low strain levels experienced as a consequence of the stiffness of the piezoelectric layers. For example, a multilayer PZT stack harvester exhibited an 18.8 mW output power at 613 Hz at extremely high accelerations (over 340 G, 1 G = 9.8 m/s^2). This yielded a power density of only 0.1 mWcm^{-3}G^{-2} [20]. Yang et al. thinned PZT plates from 300 μm to 50 μm to gain more flexibility and found that the plates curved after polishing [21]. The warped plates were made into a "gullwing"-structured PEH with a power density of 6.54 mW/cm^3 at 7.8 Hz when excited via a rotating gear. Similarly, Huang et al. bonded 400 μm PZT plate on to a Si wafer to avoid bending, and thinned the PZT to 65 μm with mechanical lapping. The acquired power density at 1012 Hz is ~0.2 mWcm^{-3}G^{-2} [22].

One aspect that would improve PEH that is missing from the literature, is the ability to readily fabricate dense piezoelectric layers with film thicknesses from 5 – 100 μm in thickness, without needing to bond and thin a bulk ceramic. Low temperature ceramic co-fire (LTCC) technologies enabled screen printing of PZT thick films on metal foils [23,24] but their electrical properties are typically not comparable with bulk ceramics and sol-gel thin films, likely due to poor densification [25] and secondary phase formation [26]. Fully sintered PZT and PMN-PT thick films from 10–100 μm were reported by Xu et al. [27] and Gentil et al. [28] via screen printing tapes on sapphire and sintering over 1100 °C. The films showed comparable performances as bulk samples, but have to be transferred to a different substrate for energy harvester applications. A sol infiltration process for the fabrication of PZT thick films yielded relative permittivity exceeding 900 with d_{33} values above 300 pC/N when crystallized around 700 °C [29,30]. While relative densities exceeding 90% have been reported by this method, the residual porosity tends to yield low in-plane piezoelectric responses (d_{31} and $e_{31,f}$). Even though some sol gel-assisted methods succeeded in fabricating PZT thick films with high $e_{31,f}$ [31], the film thicknesses rarely exceed 5 μm. As indicated by Yeo et al., thicker sol-gel PZT films necessitate long processing times, but also develop extensive micro-cracks that are detrimental to the transverse piezoelectric coefficients [14].

Thus, the principle goal of this work is to improve the mechanical and electrical properties of the tape cast PZT thick films on metal substrates such that PEH can be further optimized. This was attempted by adoption of cold sintering to break the typical thickness limitation imposed by standard film deposition methods, without sacrificing the film density. Cold sintering entails use of a transient liquid phase in conjunction with pressure, to densify a wide variety of ceramics to relative densities above 80% at temperatures below 300 °C [32–41]. This includes PZT ceramics [36,42,43], although a post-annealing step is necessary to get a pore-free and phase-pure sample with a high transverse piezoelectric coefficient. As the majority of cold sintering research concentrates on bulk ceramics, there are comparatively few demonstrations of thick film cold sintering processes [39–41]. It is anticipated that a process to fabricate bimorph, dense PZT films that are 5–50 μm thick on flexible substrates will benefit not only energy harvesting, but also multi-layer ceramic capacitors (MLCC) and multi-layer piezoelectric actuators.

2. Experimental procedure

The fabrication of PZT/metal/PZT 2–2 composites, a common configuration for cantilever PEH, can be divided into 3 phases: the preparation of PZT and substrates, the sintering of PZT/metal/PZT composites, and the characterizations of sintered composites.

2.1. Preparation of PZT tape, metal foils, and Cu tapes

The PZT powder used for this experiment is attrition-milled PZT-5A (PKI-509, Piezo Kinetics, Inc., Bellefonte, PA) with a medium particle size of ~500 nm. The milling procedures were described in the previous publication [36]. Before tape casting, 2 g PZT powder was mixed with 0.2 g $Pb(NO_3)_2$ (Sigma-Aldrich Corp., St. Louis, MO) and 1.5 mL deionized water in a mortar and pestle. The mixture was then dried in a box oven at 120 °C for 12 h. The tape cast recipe included two vehicles: vehicle A was composed of 95 wt% methyl ethyl ketone (MEK, Alfa Aesar, Tewksbury, MA) and 5 wt% poly(propylene carbonate) (QPAC®–40, Empower Materials, Inc., New Castle, DE); vehicle B consisted of 65 wt% MEK, 28 wt% QPAC®–40, and 7 wt% butyl benzyl phthalate (Santicizer-160, Tape Casting Warehouse, Inc., Morrisville, PA). The dried PZT/$Pb(NO_3)_2$ powder was mixed with 1.38 g vehicle A, 1 g MEK, and 0.68 g vehicle B with 1 min mixing between each step (Thinky Mixer AR-250, Laguna Hills, CA). After de-foaming for 30 min, the slurry was tape cast on a Mylar sheet with a blade height of ~8 mil (~203 μm) and at a speed of 8 cm/*sec*. The as-cast tape was then air dried at room temperature for 10 min to remove MEK; the final thickness of the dried tape was ~20 μm.

This work explored the use of Ni foils, Ag foils and Cu foils as substrates for the PZT films. Ni foils (25 μm, 99.99+%, Goodfellow Corporation, Coraopolis, PA) oxidize easily; if the oxygen partial pressure during firing is low enough to retain metallic Ni, Pb is reduced. $LaNiO_3/HfO_2$/Ni substrates were used to suppress the formation of NiO and reduce contact between Ni and PZT. Here HfO_2 was the passivation layer while $LaNiO_3$ (LNO) served as the bottom electrode. The processing details were similar to those described by Yeo et al. [44] except that 100 nm HfO_2 was deposited by atomic layer deposition at a rate of 0.93 Å/cycle. The silver foils (25 μm, 99.9%, Sigma-Aldrich Corp., St. Louis, MO) were cut to size and used without any further treatment. 5 layers (~100 nm) of PbO thin film were spun on to the surface of the Cu foils (25 μm, 99.8%, Alfa Aesar, Tewksbury, MA), following procedures described by Coleman et al. [45] to help provide a transient liquid phase, but no additional processing was required.

Given previous reports on constrained sintering limiting densification of ceramics on dense substrates including rigid plates and metal foils [46–49], tape cast Cu powder layers were also explored. The tape casting procedures for Cu resembles that of the PZT tape: 6.70 g Cu (Shoei Chemical, Inc., Tokyo, Japan) were mixed with 5.5 g binder containing 20 vol% QPAC®–40 and 80 vol% propylene carbonate. 0.4 mL MEK was added to the slurries in order to adjust the viscosity before the slurries were homogenized in a mixer for 3 min. The mixtures were then tape cast on Mylar sheets, followed by baking in an oven at 80 °C for 5 h to remove the solvent. The thickness of

the Cu tapes after drying was ~90 μm when the tapes were cast with a 13 mil (~330 μm) doctor blade height and a casting speed of 8 cm/s.

2.2. Cold sintering and co-firing of PZT/metal/PZT 2–2 composites

The PZT tape was cut into circular pieces one half-inch in diameter (~12.7 mm) and were stacked in a PZT/metal/PZT sandwich structure, in which one layer of PZT tape was attached on each side of the metal substrate. Lamination was done in a half-inch-diameter circular die at 50 MPa, 80 °C for 20 min [50]. The organics were then burnt out. For PZT on Ni or Ag foils, the burn out took place in a box furnace under ambient conditions with a ramp rate of 0.4 °C/min to 275 °C, a hold time of 180 min, and a cooling rate of 5 °C/min. For PZT on Cu tapes, a low pO_2 furnace with dry nitrogen, wet nitrogen and forming gas (0.1 vol% H_2 + 99.9 vol% N_2) flow ($pO_2 = 10^{-12}$ atm) was used. The temperature profile was the same as described above.

Following burn out, the samples were hung in a beaker half-filled with deionized water heated to 80 °C for 60 min. Water vapor condenses on the sample and re-moistens the lead nitrate; this is referred to as the "steaming" procedure. The stack was immediately cold sintered at 300 °C under 500 MPa uniaxial pressure for 180 min. Two pieces of 100 μm thick Kapton sheets were placed between the sample and die rams to reduce the surface roughness of the PZT. To lubricate the plunges in the die, a PTFE-contained release agent (MR311, Sprayon, Cleveland, OH) was sprayed before loading the samples.

The cold sintered PZT on Ni or Ag foils were then post-sintered at 700–900 °C with a ramp rate of 5 °C/min and a holding time of 180 min in a box furnace, while the PZT on Cu was heat treated in a tube furnace with a $pO_2 = 10^{-12}$ atm to fully sinter the PZT and Cu while reducing oxidation of Cu.

A schematic of the process flow is given in Fig. 1.

2.3. Characterization of PZT/metal/PZT 2–2 composites

The sintered sample surfaces and cross-sections were examined in a field emission scanning electron microscope (FESEM, Merlin, Carl Zeiss, Inc., Jena, Germany). Energy dispersive spectroscopy (EDS) was conducted using an Aztec detector (Oxford Instruments, High Wycombe, UK) on a NanoSEM 630 (FEI, Hillsboro, OR). The phase purity of the PZT and the substrate were assessed by X-ray diffraction (XRD, Empyrean, PANalytical Corp., Almelo, Netherlands), using Cu Kα radiation from 2θ = 10° to 72° with a step size of 0.026° 2θ and a scan rate of 0.067°/s. Fourier-transformed infrared spectroscopy (Vertex 70v FT-IR spectrometer, Bruker Scientific LLC, Billerica, MA) with a mid-IR detector (4000–400 cm^{-1}) were applied on the as cold sintered PZT on Cu tape to identify some organic impurity phases.

After processing, 2 mm diameter circular silver electrodes (Leitsiber 200, Ted Pella, Inc., Redding, CA) were painted on the sintered PZT, the permittivity-loss and polarization-electric field (P-E) hysteresis loops were measured by an LCR meter (Hewlett-Packard 4284A, Agilent Technologies, Inc., Palo Alto, CA) and a precision multiferroic analyzer (Radiant Technologies, Inc., Albuquerque, NM), respectively. The P-E loops helped determine the coercive fields (E_c) of the PZT films, which were then used to calculate the poling voltage. Samples were DC poled at room temperature under 3–4 times E_c using a pA meter (Hewlett-Packard 4140B, Agilent Technologies, Inc., Palo Alto, CA) for 20 min before piezoelectric coefficient ($e_{31,f}$) measurements. For all of the measurements, the high voltages were driven from the substrates (bottom electrodes).

The $e_{31,f}$ measurements were carried out on a custom wafer flexure station [51]. The specimens were glued on 4-inch silicon wafers, with strain gauges (KFH-1.5–120-D16-11L1M2S, gauge factor ~1.95, 7 mm by 4 mm, Omega Engineering, Inc., Norwalk, CT) attached on top of the PZT layer by super glue. Every measurement utilized two strain gauges that were perpendicular to each other. The wafers were flexed at 4 Hz via a speaker controlled by a lock-in amplifier (SR830, Stanford Research Systems, Sunnyvale, CA). A quarter Wheatstone bridge was used to process the signals from the strain gauges while a charge integration circuit collected the charges generated from the electrodes. The $e_{31,f}$ coefficient was calculated from [52]:

$$e_{31,f} = \frac{Q}{A(x_1 + x_2)} \tag{3}$$

where Q represents the charge generated from the electrode, A is the area of the electrode, and x_1, x_2 are strains in two directions.

3. Results and discussion

3.1. PZT thick films on metal foils

In initial experiments, it was found that the burnt out PZT tapes disintegrated either during steaming or when loaded into the pressing die if the samples were hand-stacked without lamination; this is likely related to the low green density and small thickness of the PZT tape. This problem could be largely ameliorated by adding a lamination step before cold sintering. Fig. 2(a) and (d) compares the 700 °C post-sintered PZT tapes on Ni foils with and without the lamination process. Lamination did not change the film microstructure significantly but it greatly suppressed the macro-flaws in the PZT layer.

A control sample was sintered at 700 °C without steaming and cold sintering to study the effects of CSP on the PZT quality. As seen in Fig. 2(d)–(g), after post-sintering the cold sintered sample presented mostly closed pores (relative density > 90% [53]), while the conventionally sintered PZT tape was still in the initial stage of

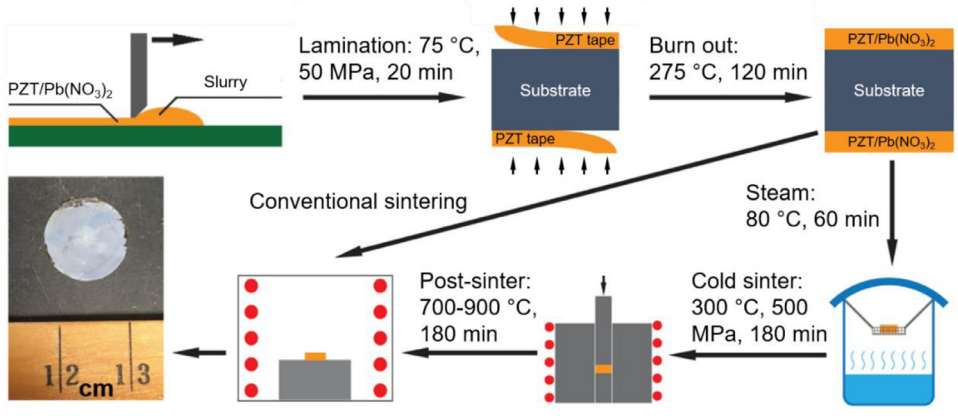

Fig. 1. Schematic flow chart for the fabrication of PZT/metal/PZT 2–2 composites. The photograph on the bottom left shows a PZT thick film on Ni foil after post-sintering.

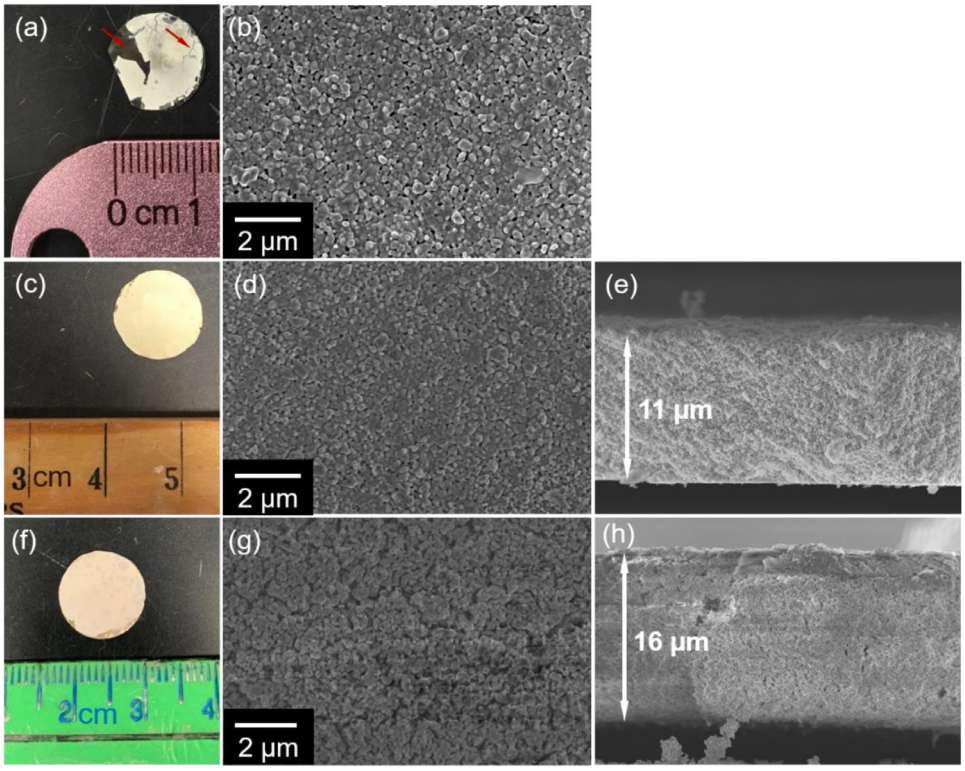

Fig. 2. (a) 700 °C post-sintered bimorph PZT thick films on LNO/HfO_2/Ni foil without use of a lamination step. The red arrows indicate regions of delamination and macro-cracks. (b) SEM image of the top PZT surface for a 700 °C post-sintered sample prepared without lamination. (c) (d) The 700 °C post-sintered sample (made with lamination), and its top surface microstructure under FESEM. (f) (g) The sample and its top surface morphology of the 700 °C post-sintered PZT tape with lamination, but without steaming and cold sintering steps. (e) (h) The cross-sectional SEM images showing the thicknesses of 700 °C post-sintered PZT tape with and without steaming and cold sintering steps, respectively.

sintering (relative density typically between 60%–65%). The cold sintered tape was a little over 10 μm thick. In contrast, the conventionally sintered PZT tape was 16 μm thick, consistent with its low density.

The dielectric permittivity and loss tangent of the PZT thick films on LNO/HfO_2/Ni foil annealed at 700 °C with and without a cold sintering step are displayed in Fig. 3(a). The cold sintered sample experienced a possible Maxwell-Wagner relaxation at 2 kHz. As shown in Fig. 3, the sample with steaming and cold sintering steps had a relative permittivity >3 times larger at 100 Hz than a conventionally sintered film and a remanent polarization improvement of nearly 7 times under the same electric field, due to improved densification. P_r of the cold sintered PZT thick film was comparable with that of 1 μm randomly-oriented 1 mol% Nb-doped PZT52/48 thin film on Pt/Ti/SiO_2/Si wafer obtained from the sol-gel method [54].

Notice that the relative permittivity of the cold sintered film is still much lower than the typical permittivity of PZT-5A [55]. The coercive field is ~2 times as high as Nb-doped PZT thin film. These results indicate the existence of residual porosity and possibly lead oxide-rich grain boundaries. In Fig. 2(d): closed pores can be seen in the sintered PZT and the grain boundaries are not clear. Consequently, after the cold sintered PZT film was poled at $3E_c$ (300 kV/cm), the measured $e_{31,f}$ was only -2.6 ± 0.01 C/m^2 (95% confidence interval), a significantly lower value than is typical of dense PZT-5A (-16 C/m^2) [55,56]. The sintered sample without CSP, however, returned zero $e_{31,f}$.

Attempts were then made to improve the density of PZT films via increasing the annealing temperature. When cold sintered PZT tapes were annealed at 900 °C, the PbO remaining from the $Pb(NO_3)_2$ melted and served as a sintering aid. [57] Previous work proved the cold sintered PZT pellet reached 99% relative density after 900 °C post-annealing for 3 h. [36] The microstructure of PZT tape annealed at 900 °C on all three types of metal foils is shown in Fig. 4(a)-(c). At 900 °C, cleaner grain boundaries

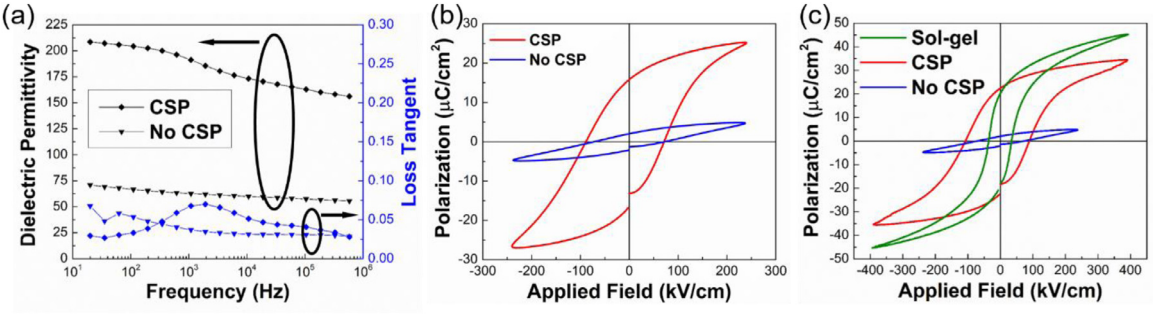

Fig. 3. (a) The relative permittivity and loss tangent of 700 °C sintered PZT thick films with and without CSP. (b) The P-E hysteresis loops of cold sintered + 700 °C post-annealed PZT thick film and 700 °C conventionally sintered PZT thick film under the same applied electric field. (c) The P-E hysteresis loops of a sol-gel Nb-PZT thin film [54], a cold sintered + 700 °C post-annealed PZT thick film, and a 700 °C conventionally sintered PZT thick film at a higher electric field. (The conventionally sintered sample broke down at fields above 250 kV/cm.).

can be observed from PZT compared with 700 °C anneal, but the density of the films was still not satisfactory. The pores are still interconnected, suggesting a relative density < 90%.

The porosity at 900 °C may be attributed to the degradation and oxidation of the Ni substrate. The XRD patterns in Fig. 5 indicates that the $LaNiO_3$ layer was mostly eliminated above 850 °C [58] while the Ni was heavily oxidized. The oxidation or cracking of Ni may have degraded the quality of the PZT film. Thickening the HfO_2 did not eliminate oxidation, suggesting that Ni foil may not be the best solution for such devices.

Annealing of cold sintered PZT/Cu/PZT specimens was carried out in a low pO_2 furnace. Unlike Ni, there is a processing window where the Cu can remain metallic while the Pb is oxidized [59]. These experiments exposed more issues on sintering PZT on metal foils. Judging from the microstructures in Fig. 4(b) and (c), porosity still existed in the PZT films. However, on Ag foil, clean grain boundaries, closed triple points, and significant grain growth were observed.

There are at least two reasons why incomplete densification was observed. First, the post-annealing temperature may be too low to allow complete densification. Secondly, the use of dense metal foils could have induced constrained sintering [60]. The second hypothesis helps explain why denser PZT films were obtained on Ag rather than on Cu: Because 900 °C is close to the melting temperature of Ag, (which could be further lowered due to the formation of Ag-PbO solid solution [61]), a thin layer of liquid phase may be formed at the interface of PZT and Ag. Therefore, the constrained sintering problem may be mitigated by the relaxation of stress at the Ag/PZT interface. However this also degraded the potential of utilizing Ag as a substrate. Silver droplets were seen on the PZT surface (marked by white arrows in Fig. 4(c)), as confirmed in the EDS in Fig. 6. These shorted the PZT film. (Notice that there are some zirconium-rich sites on the film, probably originating from either the zirconia media used during the milling of the PZT powder, or extensive lead leaching into Ag. The Al and C EDS peaks are likely from the sample holder and environmental contamination, respectively.)

It was hypothesized that if a thin layer PbO was spin cast on the surface of Cu foil, the constrained sintering issue may be relieved with the melting of PbO at 900 °C. It was found that the sintering of PZT thick film was significantly improved, except that the densification was not uniform, as shown by Fig. 4(d) and (e).

3.2. PZT thick films on tape cast Cu films

Based on the preliminary success of PZT sintering on PbO coated Cu foil, a second approach to avoiding constrained sintering is the simultaneous densification of PZT and the Cu substrate. Tape cast Cu thick films were laminated with PZT tapes and the rest of the procedures remained unchanged. In practice, it was found that the burnt out PZT/Cu tape/PZT structure is very fragile. PZT and Cu densification occurred during cold sintering, which enhanced the strength of the composites. Fig. 7(a), (c), and (e) show a high compact density of Cu and PZT after CSP, with a clean PZT-Cu interface.

Dense PZT was acquired (Fig. 7(f)) after annealing at 800 °C for 180 min in a low pO_2 furnace. This is presumably a result of good PZT and Cu compaction during CSP. And the formation of a $PbO—Cu_2O$ eutectic melt may have also contributed [62], evidenced by the formation of a thin dense layer of PZT near Cu substrate after 700 °C post-annealing (Fig. S-1 (g)). It is noted that a PZT thick film on Cu without lead nitrate failed to sinter under the same conditions (Fig. S-2), meaning that the cold sintering process is still essential. The sintered Cu layer was 40±0.91 μm thick, sandwiched between 10±0.27 μm bimorph PZT thick films (both with 95% confidence intervals), as seen in Fig. 7(b). There is still an interface between post-annealed PZT and Cu like the one shown in Fig. 7(d) which was rich in Cu and O as shown in Fig. S-3. Fig. 8 further corroborated the existence of a Cu_2O interface. The Cu_2O interface might originate from the oxidation of Cu following the decomposition of lead nitrate during burn out and cold sintering:

$$2Pb(NO_3)_2 \Leftrightarrow 2PbO + 4NO_2 + O_2 \quad (4)$$

$$4Cu + O_2 \Leftrightarrow Cu_2O \quad (5)$$

The above reactions are likely to be more complex in practice as Fig. 8 indicated an unknown peak at a low angle in the as cold sintered samples. Although difficult to index, these peaks must be from crystal structures with large lattice parameters, for example, lead hydroxyl carbonates and lead hydroxyl nitrates. The oxidation of Cu occurs at the interface between PZT and Cu, which is isolated from the external gas flow. This may explain why the Cu_2O layer cannot be removed even while processing in low pO_2 conditions. The Cu_2O intensity drop above 600 °C anneal is possibly caused by the X-ray absorption in denser PZT, since necking and grain growth appear at 600 °C, indicated in Fig. S-1 (f). At this same temperature, PbO starts to volatilize and most of it is eventually removed from the system.

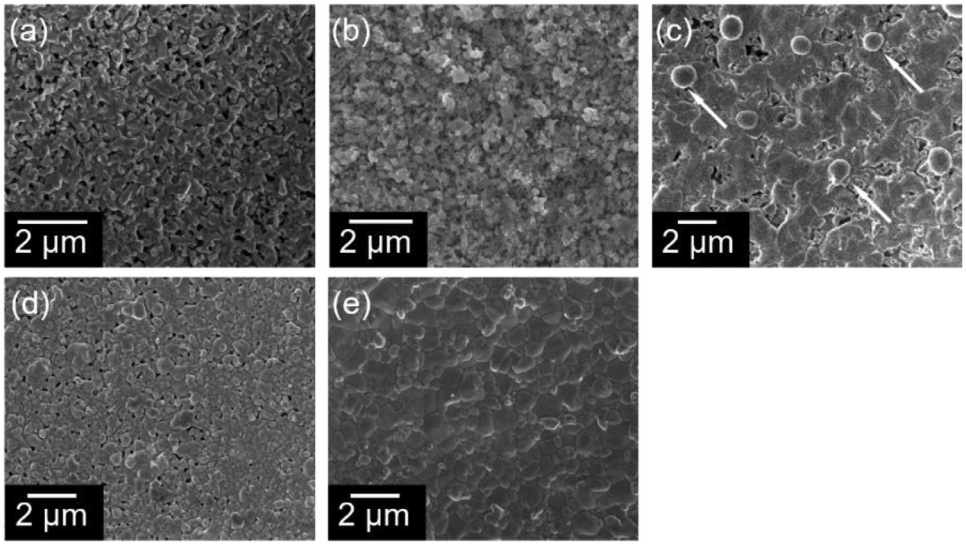

Fig. 4. SEM images of cold sintered and 900 °C-annealed PZT thick films on (a) LNO/HfO_2/Ni foil, (b) Cu foil, (c) Ag foil (Ag particles marked by arrows), and (d) (e) different regions of a PbO coated Cu foil.

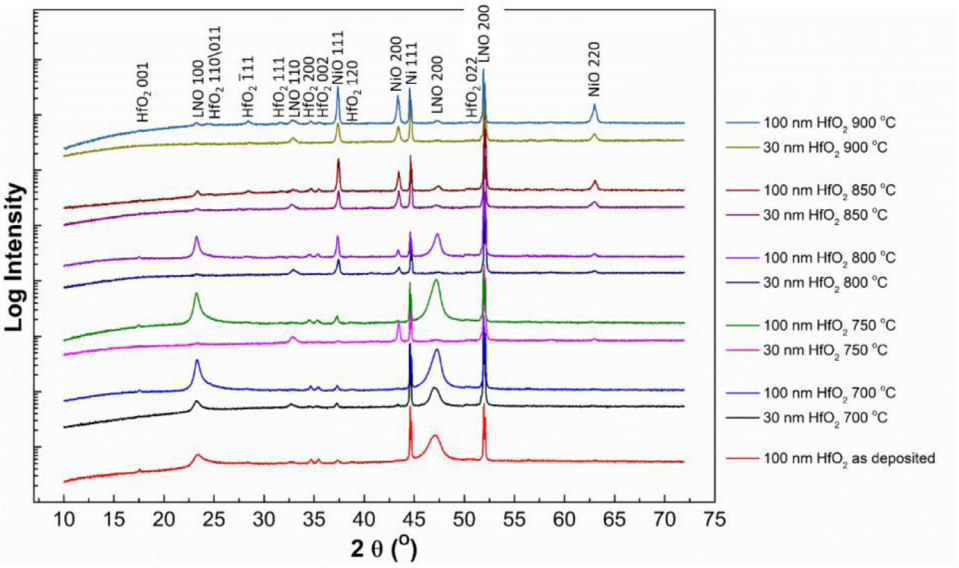

Fig. 5. XRD of the Ni foil coated by 30 nm/100 nm HfO_2 and 100 nm $LaNiO_3$ after being annealed from 700 °C to 900 °C for 180 min.

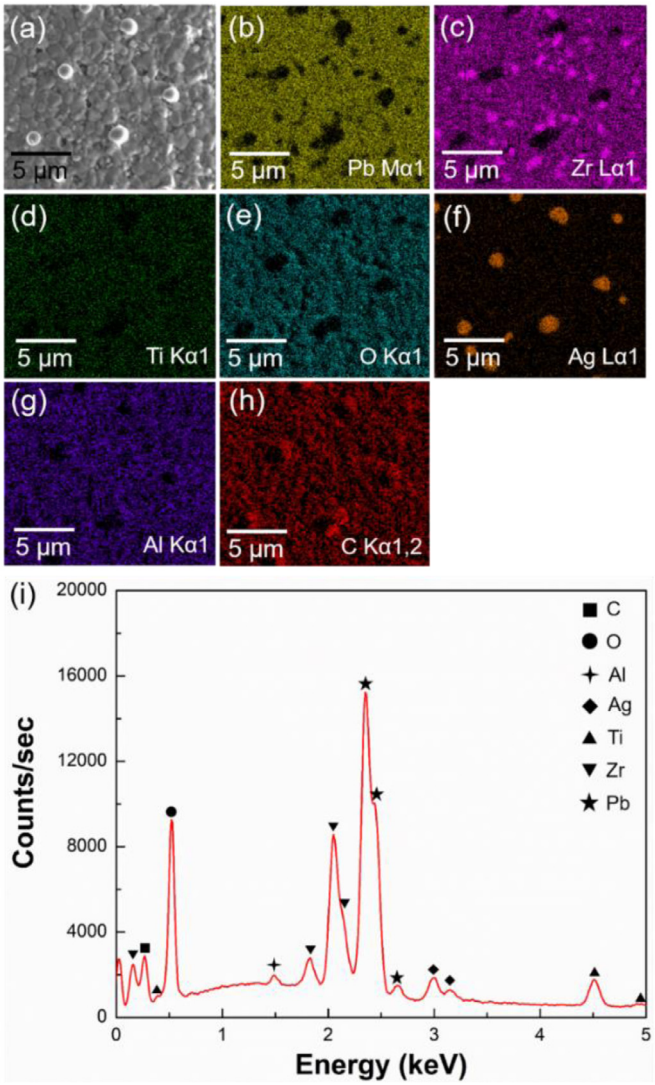

Fig. 6. (a) The top surface of 10 μm PZT thick film on Ag foil after a 900 °C, 180 min anneal. (b)-(h) The EDS mapping showing the distribution of Pb, Zr, Ti, O, Ag, Al, and C respectively. (i) The EDS spectrum of PZT surface.

Fig. 9(a) demonstrates that the relative permittivity of post-sintered PZT on Cu is 550 at 100 Hz, with a loss of 12%; these values are convolutions of the response of the PZT and the Cu_2O-rich inter-layer, and are much lower than the bulk cold sintered and post-annealed PZT discussed in the previous work [36]. The film P-E hysteresis loops were imprinted. The $+E_c$ is less than 50 kV/cm while $-E_c$ is over 75 kV/cm. This could be either due to an artifact associated with higher loss near the bottom electrode (Cu substrate), or a consequence of the depolarization fields in the Cu_2O inter-layer [63,64]. Moreover, since the post-annealing temperature of cold sintered PZT specimen is several hundred °C lower than conventional sintering conditions, the free energy for grain growth is significantly smaller,

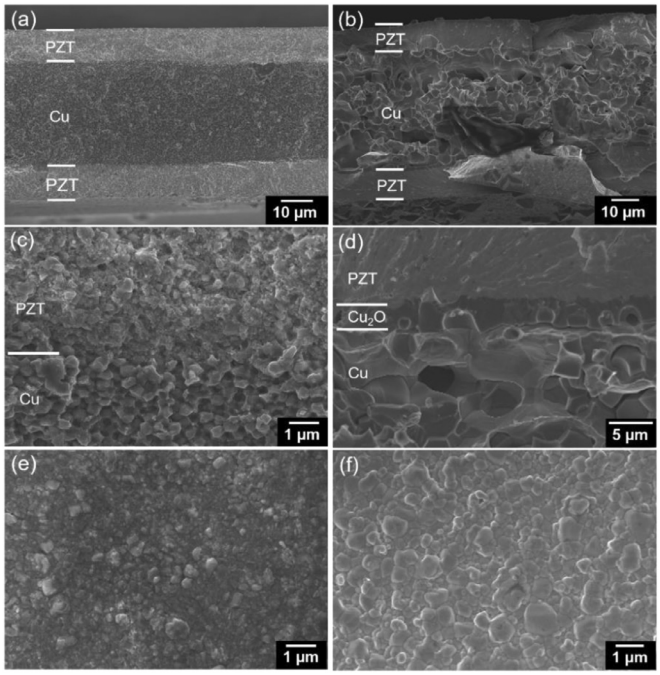

Fig. 7. (a) (b) Cross-sections of the PZT on Cu tape after CSP (left) and after 900 °C post-sintering (right) showing PZT/Cu/PZT structures. (c) (d) Zoomed in cross sections of as-cold sintered (left) and 800 °C post-sintered (right) samples emphasizing the PZT-Cu interface. (e) (f) The top surfaces of the as-cold sintered (left) and 800 °C post-sintered (right) PZT films..

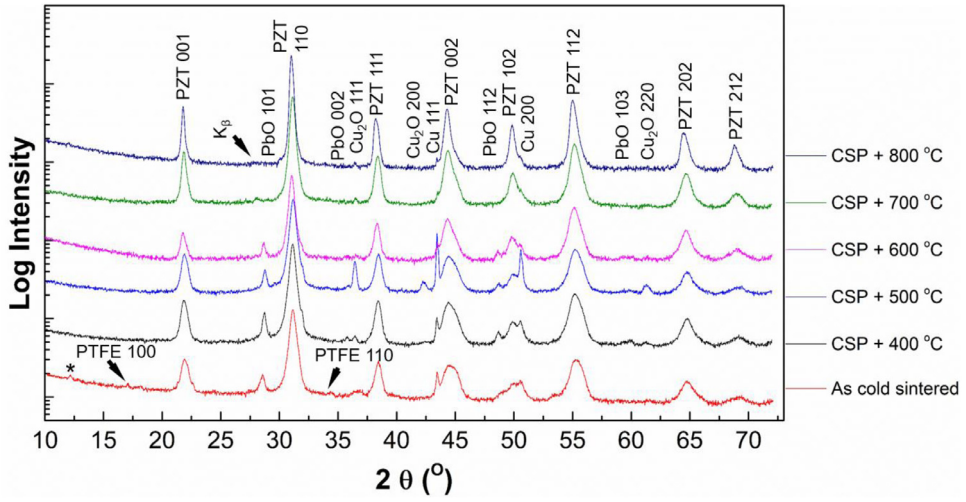

Fig. 8. The XRD patterns of as cold sintered and 400–800 °C post-annealed PZT on Cu. The unknown peaks were marked by "*". The PTFE peaks in the as cold sintered sample are most likely from the release agent mentioned in the experimental procedures to lubricate the plunges, which is corroborated by Fig. S-4.

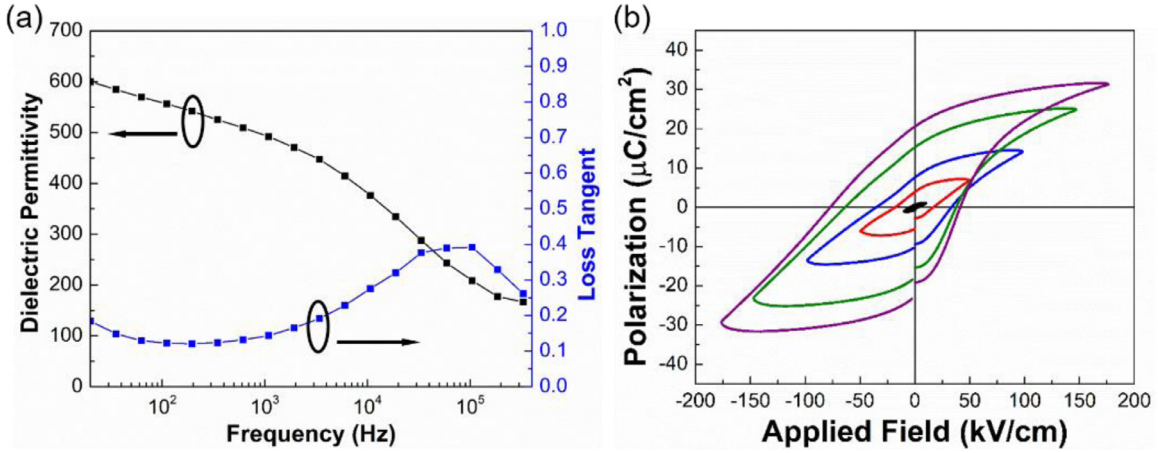

Fig. 9. (a) The relative permittivity/loss tangent under different frequencies and (b) the P-E hysteresis loops at different applied electric fields of the 800 °C post-sintered PZT on Cu tape.

resulting in inferior dielectric and piezoelectric properties [65]. Due to the inter-layer and the small grain size, the $e_{31,f}$ of the thick film was -4.7 ± 0.04 C/m^2 (95% confidence interval) after poling at 160 V ($4E_c$) at room temperature for 20 min. The electrical properties of PZT on Cu are much better than that on Ni foils, with a lower coercive field, and a larger $e_{31,f}$, though the capacitor in series was problematic. These indicate the process-property relationship of PZT films are inevitably complicated by the substrate-film interactions. The cold sintering process serves as an effective approach to controlling the densification of PZT, but further optimizations of device performance have to be addressed on grain size and substrate-PZT interfaces.

4. Conclusions

This work studied 10 μm thick film PZT/metal (Ni, Ag, and Cu) composites prepared using cold sinter-assisted processing. It was found that cracking and delamination of PZT on metal can be avoided through cold sintering. LNO/HfO_2/Ni foil has an oxidation problem and is not suitable as the substrate for PZT films; Cu foils impede the sintering of PZT tape due to constrained sintering; Ag foil substrates produced electrically shorted PZT because of high diffusivity; PbO coated Cu foil did not result in uniform densification of PZT. The film densities, relative permittivity and $e_{31,f}$ found in co-fired PZT/Cu tape make it an acceptable candidate for PZT/metal composites and potential piezoelectric energy harvesting applications.

Declaration of Competing Interest

The authors declare that they have no known competing financial interests or personal relationships that could have appeared to influence the work reported in this paper.

Acknowledgments

The research is supported by National Science Foundation (NSF) Advanced Self-Powered Systems of Integrated Sensors and Technologies (ASSIST, EEC-1160483). The authors would like to acknowledge the generosity of Empower Materials, Inc. on the binder materials for tape casting. We would also like to thanks the technical support and helpful discussions provided by Amanda Baker, Beth Jones, Dr. Jon-Paul Maria, Richard Floyd, Sarah Lowum, Beecher Watson, Kathleen Coleman, Betul Akkopru-Akgun, and Tawanda Zimudzi.

Supplementary materials

Supplementary material associated with this article can be found in the online version at doi:10.1016/j.actamat.2020.05.053.

References

[1] J. Clark, What is the internet of things?, (2016). https://www.ibm.com/blogs/internet-of-things/what-is-the-iot/.

[2] T.D. Lee, A.U. Ebong, A review of thin film solar cell technologies and challenges, Renew. Sustain. Energy Rev. 70 (2017) 1286–1297, doi: 10.1016/j.rser.2016.12.028.

[3] G.M. Joselin Herbert, S. Iniyan, E. Sreevalsan, S. Rajapandian, A review of wind energy technologies, Renew. Sustain. Energy Rev. 11 (2007) 1117–1145, doi: 10.1016/j.rser.2005.08.004.

[4] A. Uihlein, D. Magagna, Wave and tidal current energy - A review of the current state of research beyond technology, Renew. Sustain. Energy Rev. 58 (2016) 1070–1081, doi: 10.1016/j.rser.2015.12.284.

[5] E. Barbier, Nature and technology of geothermal energy: a review, Renew. Sustain. Energy Rev. 1 (1997) 1–69, doi: 10.1016/S1364-0321(97)00001-4.

[6] R. Andosca, T.G. McDonald, V. Genova, S. Rosenberg, J. Keating, C. Benedixen, J. Wu, Experimental and theoretical studies on MEMS piezoelectric vibrational energy harvesters with mass loading, Sensors Actuators A Phys 178 (2012) 76–87, doi: 10.1016/j.sna.2012.02.028.

[7] C. Dagdeviren, B.D. Yang, Y. Su, P.L. Tran, P. Joe, E. Anderson, J. Xia, V. Doraiswamy, B. Dehdashti, X. Feng, B. Lu, R. Poston, Z. Khalpey, R. Ghaffari, Y. Huang, M.J. Slepian, J.A. Rogers, Conformal piezoelectric energy harvesting and storage from motions of the heart, lung, and diaphragm, Proc. Natl. Acad. Sci. U. S. A. 111 (2014) 1927–1932, doi: 10.1073/pnas.1317233111.

[8] H.G. Yeo, T. Xue, S. Roundy, X. Ma, C. Rahn, S. Trolier-McKinstry, Strongly (001) oriented bimorph PZT film on metal foils grown by RF -sputtering for wrist-worn piezoelectric energy harvesters, Adv. Funct. Mater. 28 (2018) 1801327, doi: 10.1002/adfm.201801327.

[9] H. Liu, J. Zhong, C. Lee, S.-W. Lee, L. Lin, A comprehensive review on piezoelectric energy harvesting technology: materials, mechanisms, and applications, Appl. Phys. Rev. 5 (2018) 041306, doi: 10.1063/1.5074184.

[10] T. Xue, Ph.D. Dissertation, University of Utah, 2018.

[11] S. Priya, D.J. Inman, Energy Harvesting Technologies, Springer US, Boston, MA, 2009, doi: 10.1007/978-0-387-76464-1.

[12] P. Muralt, R.G. Polcawich, S. Trolier-McKinstry, Piezoelectric thin films for sensors, actuators, and energy harvesting, MRS Bull 34 (2009) 658–664, doi: 10.1557/mrs2009.177.

[13] C.B. Yeager, Y. Ehara, N. Oshima, H. Funakubo, S. Trolier-McKinstry, Dependence of $e_{31,f}$ on polar axis texture for tetragonal $Pb(Zr_x,Ti_{1-x})O_3$ thin films, J. Appl. Phys. 116 (2014) 104907, doi: 10.1063/1.4895339.

[14] H.G. Yeo, Ph.D. Dissertation, Pennsylvania State University, 2017.

[15] M. Akiyama, K. Umeda, A. Honda, T. Nagase, Influence of scandium concentration on power generation figure of merit of scandium aluminum nitride thin films, Appl. Phys. Lett. 102 (2013) 021915, doi: 10.1063/1.4788728.

[16] A. Erturk, D.J. Inman, An experimentally validated bimorph cantilever model for piezoelectric energy harvesting from base excitations, Smart Mater. Struct. 18 (2009) 025009, doi: 10.1088/0964-1726/18/2/025009.

[17] M. Meng, A. Ibrahim, T. Xue, H.G. Yeo, D. Wang, S. Roundy, S. Trolier-McKinstry, M. Kiani, Multi-beam shared-inductor reconfigurable voltage/SECE-mode piezoelectric energy harvesting of multi-axial human motion, in: Proceedings of the IEEE International Solid-State Circuits Conference, IEEE, 2019, pp. 426–428, doi: 10.1109/ISSCC.2019.8662414.

[18] S. Roundy, E.S. Leland, J. Baker, E. Carleton, E. Reilly, E. Lai, B. Otis, J.M. Rabaey, V. Sundararajan, P.K. Wright, Improving power output for vibration-based energy scavengers, IEEE Pervasive Comput 4 (2005) 28–36, doi: 10.1109/MPRV.2005.14.

[19] X. Ma, S. Trolier-McKinstry, C.D. Rahn, Piezoelectric compliant mechanism energy harvesters excited under large base accelerations, in: Proceedings of the ASME Design Engineering Technical Conferences, 8, 2016, doi: 10.1115/DETC201659196.

[20] T.-B. Xu, E.J. Siochi, J.H. Kang, L. Zuo, W. Zhou, X. Tang, X. Jiang, Energy harvesting using a PZT ceramic multilayer stack, Smart Mater. Struct. 22 (2013) 1–15, doi: 10.1088/0964-1726/22/6/065015.

[21] B. Yang, Z. Yi, G. Tang, J. Liu, A gullwing-structured piezoelectric rotational energy harvester for low frequency energy scavenging, Appl. Phys. Lett. 115 (2019) 063901, doi: 10.1063/1.5110368.

[22] M. Huang, C. Hou, Y. Li, H. Liu, F. Wang, T. Chen, Z. Yang, G. Tang, L. Sun, A low-frequency MEMS piezoelectric energy harvesting system based on frequency up-conversion mechanism, Micromachines (Basel) 10 (2019) 639, doi: 10.3390/mi10100639.

[23] A. Lozinski, F. Wang, A. Uusimäki, S. Leppävuori, PLZT thick films for pyroelectric sensors, Meas. Sci. Technol. 8 (1997) 33–37, doi: 10.1088/0957-0233/8/1/005.

[24] S. Le Dren, L. Simon, P. Gonnard, M. Troccaz, A. Nicolas, Investigation of factors affecting the preparation of PZT thick films, Mater. Res. Bull. 35 (2000) 2037–2045, doi: 10.1016/S0025-5408(00)00402-5.

[25] R.A. Dorey, R.W. Whatmore, S.P. Beeby, R.N. Torah, N.M. White, Screen printed PZT thick films using composite film technology, Integr. Ferroelectr. 54 (2003) 651–658, doi: 10.1080/10584580390259065.

[26] A. Wu, P. Vilarinho, S. Srinivasan, A. Kingon, I. Reaney, D. Woodward, A. Ramos, E. Alves, Microstructural studies of PZT thick films on Cu foils, Acta Mater 54 (2006) 3211–3220, doi: 10.1016/j.actamat.2006.03.006.

[27] Baomin Xu, S. Buhler, D. White, J. Zesch, W. Wong, Fabrication of piezoelectric thick films for high frequency transducers, in: Proceedings of the IEEE Symposium on Ultrasonic, IEEE, 2003, pp. 1999–2002, doi: 10.1109/ULTSYM.2003.1293309.

[28] S. Gentil, D. Damjanovic, N. Setter, $Pb(Mg_{1/3}Nb_{2/3})O_3$ and (1-x)$Pb(Mg_{1/3}Nb_{2/3})O_3$-x$PbTiO_3$ relaxor ferroelectric thick films: processing and electrical characterization, J. Electroceramics 12 (2004) 151–161, doi: 10.1023/B:JECR.0000037720.39443.e3.

[29] T.Y. Kwon, J.H. Park, Y.B. Kim, D.S. Yoon, C. Il Cheon, H.L. Lee, T.S. Kim, Preparation of piezoelectric 0.1$Pb(Zn_{0.5}W_{0.5})O_3$–0.9$Pb(Zr_{0.5}Ti_{0.5})O_3$ solid solution and thick films for low temperature firing on a Si-substrate, J. Cryst. Growth. 295 (2006) 172–178, doi: 10.1016/j.jcrysgro.2006.07.005.

[30] D.A. Barrow, T.E. Petroff, R.P. Tandon, M. Sayer, Characterization of thick lead zirconate titanate films fabricated using a new sol gel based process, J. Appl. Phys. 81 (1997) 876–881, doi: 10.1063/1.364172.

[31] D. Wu, Q. Zhou, K.K. Shung, S.N. Bharadwaja, D. Zhang, H. Zheng, Dielectric and piezoelectric properties of PZT composite thick films with variable solution to powder ratios, J. Am. Ceram. Soc. 92 (2009) 1276–1279, doi: 10.1111/j.1551-2916.2009.03065.x.

[32] H. Kahari, M. Teirikangas, J. Juuti, H. Jantunen, Dielectric properties of lithium molybdate ceramic fabricated at room temperature, J. Am. Ceram. Soc. 97 (2014) 3378–3379, doi: 10.1111/jace.13277.

[33] H. Guo, J. Guo, A. Baker, C.A. Randall, Hydrothermal-assisted cold sintering process: a new guidance for low-temperature ceramic sintering, ACS Appl. Mater. Interfaces. 8 (2016) 20909–20915, doi: 10.1021/acsami.6b07481.

[34] J. Guo, B. Legum, B. Anasori, K. Wang, P. Lelyukh, Y. Gogotsi, C.A. Randall, Cold sintered ceramic nanocomposites of 2D MXene and zinc oxide, Adv. Mater. 30 (2018) 1–6, doi: 10.1002/adma.201801846.

[35] S. Funahashi, J. Guo, H. Guo, K. Wang, A.L. Baker, K. Shiratsuyu, C.A. Randall, Demonstration of the cold sintering process study for the densification and grain growth of ZnO ceramics, J. Am. Ceram. Soc. 100 (2017) 546–553, doi: 10.1111/jace.14617.

[36] D. Wang, H. Guo, C.S. Morandi, C.A. Randall, S. Trolier-McKinstry, Cold sintering and electrical characterization of lead zirconate titanate piezoelectric ceramics, APL Mater 6 (2018) 016101, doi: 10.1063/1.5004420.

[37] J.P. Maria, X. Kang, R.D. Floyd, E.C. Dickey, H. Guo, J. Guo, A. Baker, S. Funihashi, C.A. Randall, Cold sintering: current status and prospects, J. Mater. Res. 32 (2017) 3205–3218, doi: 10.1557/jmr.2017.262.

[38] S.S. Faouri, A. Mostaed, J.S. Dean, D. Wang, D.C. Sinclair, S. Zhang, W.G. Whittow, Y. Vardaxoglou, I.M. Reaney, High quality factor cold sintered Li_2MoO_4–$BaFe_{12}O_{19}$ composites for microwave applications, Acta Mater 166 (2019) 202–207, doi: 10.1016/j.actamat.2018.12.057.

[39] H. Kähäri, P. Ramachandran, J. Juuti, H. Jantunen, Room-temperature densified Li_2MoO_4 ceramic patch antenna and the effect of humidity, Int. J. Appl. Ceram. Technol. 14 (2017) 50–55, doi: 10.1111/ijac.12615.

[40] J.-H. Seo, K. Verlinde, J. Guo, D.S.B. Heidary, R. Rajagopalan, T.E. Mallouk, C.A. Randall, Cold sintering approach to fabrication of high rate performance binderless $LiFePO_4$ cathode with high volumetric capacity, Scr. Mater. 146 (2018) 267–271, doi: 10.1016/j.scriptamat.2017.12.005.

[41] T. Hérisson de Beauvoir, S. Dursun, L. Gao, C.A. Randall, New opportunities in metallization integration in co-fired electroceramic multilayers by the cold sintering process, ACS Appl. Electron. Mater. (2019), doi: 10.1021/acsaelm.9b00184.

[42] M. Nelo, T. Siponkoski, H. Kähäri, K. Kordas, J. Juuti, H. Jantunen, Upside-down composites, Fabricating piezoceramics at room temperature, J. Eur. Ceram. Soc. 39 (2019) 3301–3306, doi: 10.1016/j.jeurceramsoc.2019.04.052.

[43] M. Suzuki, H. Ushijima, T. Tsuchiya, J. Akedo, Polarization properties of aggregate PZT films produced at room temperature, in: K. Kato, G. Brennecka (Eds.), Proceedings of the 19th US-Japan Seminar on Dielectric, Piezoelectric Ceram., Tsukuba, Japan, 2019, pp. 147–148.

[44] H.G. Yeo, S. Trolier-McKinstry, {001} Oriented piezoelectric films prepared by chemical solution deposition on Ni foils, J. Appl. Phys. 116 (2014) 014105, doi: 10.1063/1.4886597.

[45] K. Coleman, J. Walker, T. Beechem, S. Trolier-McKinstry, Effect of stresses on the dielectric and piezoelectric properties of $Pb(Zr_{0.52}Ti_{0.48})O_3$ thin films, J. Appl. Phys. 126 (2019) 034101, doi: 10.1063/1.5095765.

[46] R.K. Bordia, R. Raj, Sintering behavior of ceramic films constrained by a rigid substrate, J. Am. Ceram. Soc. 68 (1985) 287–292, doi: 10.1111/j.1151-2916.1985.tb15227.x.

[47] A. Mohanram, S.-H. Lee, G.L. Messing, D.J. Green, Constrained sintering of low-temperature co-fired ceramics, J. Am. Ceram. Soc. 89 (2006) 1923–1929, doi: 10.1111/j.1551-2916.2006.01079.x.

[48] S.-Y. Tzeng, J.-H. Jean, Stress development during constrained sintering of alumina/glass/alumina sandwich structure, J. Am. Ceram. Soc. 85 (2004) 335–340, doi: 10.1111/j.1151-2916.2002.tb00093.x.

[49] A. Wu, P.M. Vilarinho, A.I. Kingon, Electrophoretic deposition of lead zirconate titanate films on metal foils for embedded components, J. Am. Ceram. Soc. 89 (2006) 575–581, doi: 10.1111/j.1551-2916.2005.00732.x.

[50] L. Gao, S.W. Ko, H. Guo, E. Hennig, C.A. Randall, J.L. Jones, Demonstration of copper co-fired (Na,K)NbO_3 multilayer structures for piezoelectric applications, J. Am. Ceram. Soc. 99 (2016) 2017–2023, doi: 10.1111/jace.14207.

[51] J.F. Shepard, P.J. Moses, S. Trolier-McKinstry, The wafer flexure technique for the determination of the transverse piezoelectric coefficient (d_{31}) of PZT thin films, Sensors Actuators A Phys 71 (1998) 133–138, doi: 10.1016/S0924-4247(98)00161-7.

[52] L.M. Garten, S. Trolier-McKinstry, The field induced $e_{31,f}$ piezoelectric and Rayleigh response in barium strontium titanate thin films, Appl. Phys. Lett. 105 (2014) 132905, doi: 10.1063/1.4897299.

[53] M.N. Rahaman, Ceramic Processing and Sintering, 2nd ed., Marcel Dekker, New York, NY, 2003 https://books.google.com/books?id=qgpEDwAAQBAJ&printsec=frontcover&dq=inauthor:%22Mohamed+N.+Rahaman%22&hl=en&sa=X&ved=0ahUKEwjLrMeYgJrjAhUJH80KHc6HBLQQ6AEIKjAA#v=onepage&q&f=false .

[54] B. Akkopru–Akgun, W. Zhu, M.T. Lanagan, S. Trolier–McKinstry, The effect of imprint on remanent piezoelectric properties and ferroelectric aging of $PbZr_{0.52}Ti_{0.48}O_3$ thin films, J. Am. Ceram. Soc. 102 (2019) 5328–5341, doi: 10.1111/jace.16367.

[55] A. Erturk, D.J. Inman, Piezoelectric Energy Harvesting, John Wiley & Sons, Ltd, Chichester, UK, 2011, doi: 10.1002/9781119991151.
[56] M.-A. Dubois, P. Muralt, Measurement of the effective transverse piezoelectric coefficient $e_{31,f}$ of AlN and $Pb(Zr_xTi_{1-x})O_3$ thin films, Sensors Actuators A Phys 77 (1999) 106–112, doi: 10.1016/S0924-4247(99)00070-9.
[57] R.B. Atkin, R.M. Fulrath, Point defects and sintering of lead zirconate-titanate, J. Am. Ceram. Soc. 54 (1971) 265–270, doi: 10.1111/j.1151-2916.1971.tb12286.x.
[58] A. Li, C. Ge, P. Lü, N. Ming, Preparation of perovskite conductive $LaNiO_3$ films by metalorganic decomposition, Appl. Phys. Lett. 68 (1996) 1347–1349, doi: 10.1063/1.115930.
[59] L. Gao, H. Guo, S. Zhang, C. Randall, Base metal co-fired multilayer piezoelectrics, Actuators 5 (2016) 8, doi: 10.3390/act5010008.
[60] P.J. Holmes, R.G. Loasby, Handbook of Thick Film Technology, Electrochemical Publications, 1976.
[61] Z.B. Shao, K.R. Liu, L.Q. Liu, H.K. Liu, S. Dou, Equilibrium phase diagrams in the systems PbO-Ag and CuO-Ag, J, Am. Ceram. Soc. 76 (1993) 2663–2664, doi: 10.1111/j.1151-2916.1993.tb03996.x.
[62] D.L. Corker, R.W. Whatmore, E. Ringgaard, W.W. Wolny, Liquid-phase sintering of PZT ceramics, J. Eur. Ceram. Soc. 20 (2000) 2039–2045, doi: 10.1016/S0955-2219(00)00089-3.
[63] R.R. Mehta, B.D. Silverman, J.T. Jacobs, Depolarization fields in thin ferroelectric films, J. Appl. Phys. 44 (1973) 3379–3385, doi: 10.1063/1.1662770.
[64] P. Wurfel, I.P. Batra, Depolarization effects in thin ferroelectric films, Ferroelectrics 12 (1976) 55–61, doi: 10.1080/00150197608241393.
[65] C.a Randall, N. Kim, J.-P. Kucera, W. Cao, T.R. Shrout, Intrinsic and extrinsic size effects in fine-grained morphotropic-phase-boundary lead zirconate titanate ceramics, J. Am. Ceram. Soc. 81 (2005) 677–688, doi: 10.1111/j.1151-2916.1998.tb02389.x.